Thalamic spontaneous activity coordinates the timing of corticothalamic innervation in the visual system

Verónica Moreno-Juan, Francisco J. Martini, Leticia Pérez-Saiz, Álvaro Herrero-Navarro, Miguel Valdeolmillos and Guillermina López-Bendito*

Instituto de Neurociencias de Alicante, Universidad Miguel Hernández-Consejo Superior de Investigaciones Científicas (UMH-CSIC), Sant Joan d'Alacant, Spain.

***Correspondence:** g.lbendito@umh.es

Summary

Sensory processing relies on the correct development of circuits connecting thalamus and cortex. Visual corticothalamic axons (CTAs) invade the thalamic dorsolateral geniculate nucleus (dLGN) of the thalamus following an early postnatal time-regulated programme in mice. Retinal spontaneous activity influences the thalamic incursion of CTAs, however, the perinatal thalamus also generates intrinsic patterns of spontaneous activity whose role in modulating afferent connectivity remains unknown. Here, we found that patterned spontaneous activity in the dLGN is critical for the proper spatial and temporal innervation of CTAs. When the spontaneous dLGN activity is disrupted *in vivo*, CTA innervation is severely delayed until eye-opening. Indeed, visual input influenced the temporal development of CTAs by modulating thalamic activity, as embryonic enucleation enhanced thalamic calcium waves and accelerated the entrance of CTAs into the dLGN. Our results show that patterned spontaneous activity in the perinatal thalamus is a key element driving the wiring of visual circuits.

Keywords

Thalamus, development, corticogeniculate, corticothalamic, thalamocortical, spontaneous activity, retinal input.

Introduction

The formation of sensory circuits relies on the highly regulated spatial and temporal organization of axon connectivity. The visual system has been used extensively as a model to decipher the processes that control the development of neuronal networks, such as axon guidance and/or targeting. Indeed, retinofugal projections have been employed to study in some detail how topographic organization is established in the visual pathway (Fox & Guido, 2011; Huberman et al., 2008; Shatz & Rakic, 1981a; Zipursky & Sanes, 2010). The development of the visual system in mice, depends on feed-forward input from the retina through the retinothalamic axons (RTAs) that reach the dorsolateral geniculate nucleus (dLGN) of the thalamus on embryonic day 15 (E15), ensuring that ipsilateral and contralateral axon segregation is completed by postnatal day 8 (P8: Godement, Salaün, & Imbert, 1984a). By contrast, corticothalamic axons (CTAs) from layer 6 (L6) of the primary visual cortex (V1) reach the dorsal border of the dLGN at E18 and they begin to invade this nucleus around P4. Indeed, after the first postnatal week, CTAs have colonized the entire dLGN (Brooks et al., 2013; Grant, Hoerder-Suabedissen, & Molnár, 2016; Seabrook, El-Danaf, Krahe, Fox, & Guido, 2013).

Numerically, CTAs represent the largest input to the dLGN and it has been demonstrated that they are key regulators of dLGN cell firing (Erişir, Bickford, Van Horn, & Sherman, 1997; Godwin et al., 1996; McCormick & Krosigk, 1992). However, the feedback from the V1 to dLGN develops relatively late with respect to the retinal inputs (Drager & Hubel, 1975; Godement, Salaün, & Imbert, 1984b; Grant et al., 2016; Jacobs et al., 2007; Seabrook et al., 2013; Shatz & Rakic, 1981b). It has been suggested that RTAs and CTAs might interact to ensure the correct development of both projections during the second postnatal week (Bickford et al., 2009; Seabrook et al.,

2013). More recent insights into this process demonstrate that the invasion of the dLGN by cortical and retinal inputs relies on their mutual interactions at the thalamus (Brooks et al., 2013; Grant et al., 2016; Jurgens, Bell, McQuiston, & Guido, 2012; Seabrook et al., 2013; Thompson, Gribizis, Chen, & Crair, 2017). These interactions seem to be activity-dependent, as disrupting postnatal retinal waves by injecting the cholinergic agonist epibatidine accelerates CTA entry into the dLGN (Grant et al., 2016). Indeed, postnatal enucleation of mice leads to earlier innervation of the dLGN by CTAs (Brooks et al., 2013; Grant et al., 2016; Seabrook et al., 2013). These results suggest that early peripheral input and the electric messages conveyed are key elements for the timely innervation and correct development of CTAs in the visual pathway. However, retinal waves are not the only activity that trains the developing thalamus. It was recently shown that the perinatal thalamus generates an intrinsic pattern of spontaneous activity that is known to regulate the organization of sensory systems (Antón-Bolaños et al., 2019; Castillo-Paterna et al., 2015; Mire et al., 2012; Moreno-Juan et al., 2017), suggesting this activity may possibly regulate the innervation of the dLGN. Here, we tested this hypothesis using an *in vivo* approach in which thalamic spontaneous activity is modified in the dLGN. We found that alterations to the patterns of spontaneous thalamic activity in the dLGN during prenatal and postnatal stages impair the timing of CTA innervation of this nucleus. Remarkably, the absence of CTAs in the dLGN is rescued by eye opening, strongly suggesting that both intrinsic spontaneous activity and experience-dependent programmes play a role in the development of the corticothalamic circuits associated with the visual system.

Results

Disrupting the pattern of spontaneous activity in the developing visual thalamus

To determine whether innervation of the dLGN by visual CTAs requires thalamic spontaneous activity, we disrupted the activity of the thalamus by overexpressing the inward rectifier potassium channel 2.1 (Kir2.1) in all the principal thalamic sensory nuclei. As such, we administered tamoxifen to pregnant *Gbx2*^{CreER};*R26*$^{Kir2.1\text{-}floxed}$ mice (referred herein as *Th*^{Kir}) when embryos were at E10.5, inducing the overexpression of Kir2.1 (fused to mCherry) in embryonic thalamic neurons (Antón-Bolaños et al., 2019). As expected, the increase in Kir2.1 suppressed the patterned spontaneous activity in the dLGN of new-born *Th*^{Kir} mice, this activity normally evident as calcium waves (**Figure 1A-D**: Moreno-Juan et al., 2017). Calcium imaging of *ex vivo* brain slices from *Th*^{Kir} mice at P0 demonstrated that neurons from the dLGN only activated asynchronously, with no large and propagating co-activation witnessed, such as that recorded in control slices. Therefore, and as shown previously for the somatosensory and auditory nuclei of the thalamus (Moreno-Juan et al., 2017; Antón-Bolaños et al., 2019), overexpression of Kir2.1 transforms the pattern of dLGN activity from synchronous to asynchronous at perinatal stages. Towards the end of the first postnatal week, an additional change in the pattern of spontaneous activity was recorded in the *Th*^{Kir} mice *in vivo*. Extracellular recordings with multichannel electrodes in the thalamus revealed that the firing rate of dLGN neurons decreased significantly in the *Th*^{Kir} mice at P6 (**Figure 1E-H**). Therefore, there is *ex vivo* and *in vivo* evidence that the overexpression of Kir2.1 alters the properties of spontaneous activity in the visual thalamus during the initial days post-partum, the time when CTAs reach and invade the dLGN.

Thalamic spontaneous activity mediates the entry of CTAs into the dLGN

97 In light of the above, we determined whether an abnormal intrinsic pattern of
98 spontaneous activity in the thalamus could affect the progression of CTAs into the
99 dLGN. As such, we visualized CTAs in the dLGN through their expression of the
100 vGlut1 transporter expressed at the terminals of corticothalamic neurons (Grant et al.,
101 2016; Piñon, Jethwa, Jacobs, Campagnoni, & Molnár, 2009; Varoqui, Schäfer, Zhu,
102 Weihe, & Erickson, 2002), as well as in the transgenic mouse line *Golli-tau-eGfp* that
103 labels cortical L6 neurons and their axons (Grant et al., 2016; Jacobs et al., 2007). At
104 P3, control axons from L6 appeared adjacent to the ventromedial border of the dLGN,
105 progressively invading the nucleus over successive days (**Figure S1**: Brooks et al.,
106 2013). While control CTAs had already entered the dLGN by P4, they remained at the
107 border in the Th^{Kir} mice (**Figure 2A**). In addition, we also measured the invasion of
108 CTAs in the dLGN in terms of the vGlut1 fluorescence in the dLGN area of control and
109 Th^{Kir} mice at P4, P6 and P9. The invasion of the dLGN by CTAs was severely perturbed
110 in the Th^{Kir} mice and while CTAs covered more than half of the nucleus in control
111 animals at P9, the invasion of this territory by CTAs was reduced by more than 90%
112 when thalamic spontaneous activity was disturbed (**Figure 2B**). This result was
113 confirmed by labelling L6 neurons from the V1 with a lentivirus expressing *Gfp*,
114 showing that virtually no CTAs had invaded the dLGN in Th^{Kir} mice at P9 (**Figure 2C**).
115 This effect was not due to a developmental delay in the arrival of CTAs in these Th^{Kir}
116 mice since L6 axons appear to be waiting at the border of the dLGN in both the control
117 and Th^{Kir} mice at P0 (**Figure 2D**). Together these results indicate that spontaneous
118 activity in the dLGN regulates the invasion of this structure by CTAs.
119
120 **Disrupting the patterned thalamic activity leads dLGN neuron death**

121 When analysing CTA invasion in the *Th*^{Kir} mice, we noticed that perturbing
122 spontaneous thalamic activity provoked a decrease in the size of the dLGN. While the
123 dLGN size was normal in *Th*^{Kir} mice from P0 to P3, it remained stationary from P4
124 onwards, a period in which the size of the dLGN normally increased in control mice and
125 when the CTAs invaded the thalamus (**Figure 3A**). To determine whether this lack of
126 growth of the dLGN is due to an increase in cell-death and/or the enhanced compaction
127 of dLGN cells, we analysed caspase-3a activity (Ahern et al., 2013; Lossi, Castagna, &
128 Merighi, 2015) and the cell density in the dLGN of control and *Th*^{Kir} mice. There was a
129 significant increase in caspase-3a immunostaining from P3 to P6 in the dLGN of the
130 *Th*^{Kir} mice (**Figure 3B and 3C**) but no increase in cell density in this nucleus (**Figure**
131 **S2A and S2B**). Hence, these data suggest that the failure to increase the size of the
132 dLGN in the *Th*^{Kir} mice might be the result of enhanced cell-death in this nucleus, in
133 conjunction with an absence of CTAs in the visual thalamus.
134
135 **The lack of innervation of the dLGN by CTAs is independent of RTAs**
136 It was previously suggested that a hierarchy exists in the temporal invasion of the dLGN
137 by afferent axons, with RTAs preceding CTAs (Brooks et al., 2013; Guido, 2018;
138 Jacobs et al., 2007; Seabrook et al., 2013). Furthermore, it was suggested that cortical
139 input from L6 neurons is required for the correct targeting of RTAs to the dLGN and for
140 their eye-specific segregation (Shanks et al., 2016; Thompson, Picard, Min, Fagiolini, &
141 Chen, 2016). Therefore, the mechanisms defining axon interactions might regulate the
142 invasion of the dLGN by these two sets of projections, whereby RTAs are reorganized
143 and segregated once CTAs start to innervate the dLGN. Indeed, Cholera-Toxin subunit
144 B (CTB) injections into the eyes of *Golli-tau-eGfp* mice revealed that RTAs preceded
145 CTA innervation of the dLGN (**Fig. 4A** and **4B**), supporting previous findings

146 (Seabrook et al., 2013). As perturbed thalamic spontaneous activity strongly affects the
147 innervation of the dLGN by CTAs, we tested whether the absence of CTAs in the Th^{Kir}
148 mouse is a consequence of an early defect in RTA innervation. As such, we performed
149 anterograde labelling of RTAs by injecting Alexa-647 conjugated CTB into the retina.
150 Remarkably, we found that the timing of contralateral and ipsilateral RTA invasion of
151 the dLGN is normal at P2 in Th^{Kir} mice (**Figure 4C and 4D**). Hence, retinal axons
152 target and invade the dLGN independently of thalamic activity and the absence of CTAs
153 in the dLGN is not due to a defect of the RTAs.
154

155 **Retinal inputs modify the spontaneous thalamic activity in the dLGN**

156 Our previous results demonstrated that normal spontaneous activity in the dLGN is
157 required for CTAs to invade this nucleus. Interestingly, the pattern of the spontaneous
158 activity in the somatosensory nucleus of the thalamus is thought to be modified after the
159 removal of retinal input due to embryonic bilateral enucleation (embBE: Moreno-Juan
160 et al., 2017). Hence, we cannot rule out that the presence of RTAs might somehow also
161 influence spontaneous activity in the visual thalamus and thereby affect the
162 development of CTAs. In fact, postnatal deprivation of the visual periphery input
163 provokes an aberrant development of the CTAs in the dLGN (Grant et al., 2016; Jacobs
164 et al., 2007; Seabrook et al., 2013). To test this possibility, we performed embryonic
165 bilateral enucleations at E14.5 to ensure that visual input never reached the thalamus, as
166 retinal axons reach the dLGN at E15.5 in mice (Moreno-Juan et al., 2017). To detect the
167 spontaneous activity in the dLGN, we performed calcium imaging *ex vivo* in control and
168 embBE slices at P1, prior to CTA invasion of the dLGN (**Figure 5A and Figure 5E**).
169 At this stage we found a higher frequency of spontaneous synchronous calcium events
170 in the dLGN of embBE mice, which included the appearance of more thalamic calcium

171 waves than in control mice (**Figure 5B and 5C**). As such, these experiments show that
172 despite the emergence of thalamic waves that are independent of retinal input, RTAs
173 exert a modulatory role on the patterned activity of the dLGN that is revealed in
174 enucleated animals.

175 We next determined whether innervation of the dLGN by CTAs is affected in
176 embBE mice by performing enucleations at E14.5 in wild-type and *Golli-tau-eGfp* mice
177 (**Figure 5D**). In control animals, CTAs began to invade the dLGN from P4 and they
178 have covered the entire nucleus by around P12, close to the time of eye-opening
179 (Brooks et al., 2013; Seabrook et al., 2013). By contrast, in embBE mice CTAs
180 expressing GFP or labelled for vGlut1 immunostaining already covered a significantly
181 higher proportion of the dLGN (8.85%) at P1 than in their control littermates (3.25%).
182 This acceleration of dLGN invasion was maintained at all the developmental stages
183 studied (P2, P3 and P7: **Figure 5E** and **5F, Figure S3**), and it was in accordance with
184 data found previously in mice enucleated at P0 (Brooks et al., 2013; Grant et al., 2016;
185 Seabrook et al., 2013).

186 These results show that the arrival of retinal axons has strong impact on the
187 developing dLGN. First, they regulate the pattern of spontaneous activity and secondly,
188 they influence the postnatal innervation of the dLGN by CTAs. However, it remains
189 unclear whether there is a causal link between these events. In order to address this
190 question, we performed bilateral embryonic enucleations in the Th^{Kir} mice (**Figure 5G**).
191 Remarkably, we found that CTA innervation of the dLGN is rescued when RTAs are
192 eliminated in Th^{Kir} mice. The relative invasion of the dLGN by CTAs in the embBE
193 Th^{Kir} mice was similar to that of embBE mice (**Figure 5H and 5I**), demonstrating the
194 existence of a hierarchical organization in the invasion of the dLGN whereby the arrival

195 of RTAs switches the pattern of spontaneous activity in the nucleus, in turn, delaying
196 the entry of CTAs.
197
198 **Visual experience rescues CTA innervation of the dLGN in the *Th^{Kir}* mice**
199 Our results demonstrated that altering the patterns of early thalamic spontaneous
200 activity affects the development of the corticothalamic connections to the dLGN. The
201 reduction in spontaneous dLGN activity due to the absence of thalamic calcium waves
202 induced a severe defect in CTA innervation, which were virtually absent from the
203 dLGN during the first postnatal week, and at least until P9. Nevertheless, as *Th^{Kir}* mice
204 survive until adulthood, we wondered whether this effect might persist. Notably, at P30
205 CTAs had innervated the full extent of the dLGN in *Th^{Kir}* mice as in control littermates
206 (**Figure S4A**), indicating that the aberrant CTA innervation detected early in
207 development is reversed at later stages.
208 Eye-opening occurs in mice at around P13, an event that is crucial for the final
209 maturation and refinement of the visual system (Hensch, 2005; Hofer, Mrsic-Flogel,
210 Bonhoeffer, & Hübener, 2009; Hooks & Chen, 2006; Pecka, Han, Sader, & Mrsic-
211 Flogel, 2014). As CTA invasion of the dLGN is rescued after P9, we assessed whether
212 eye-opening might play a role in this recovery. We analysed the innervation of the
213 dLGN by CTAs in both control and *Th^{Kir}* mice at P10, P13 and P14, just before and
214 after eye-opening. We found that while at P10 when the eyes are still closed, CTAs
215 poorly innervated the dLGN in *Th^{Kir}* mice relative to the controls (**Figure 6A)**.
216 However, after eye-opening, the CTA invasion in *Th^{Kir}* mice at P13-P14 was
217 indistinguishable from that of the control mice (**Figure 6B and S4B**).
218 Visual stimulation through close eyelids evokes glutamatergic retinal waves, and
219 light deprivation in mice from P8 to P14 provokes deficient retinogeniculate

220 segregation, demonstrating that activity derived by light stimulus just prior to eye
221 opening influences the topographic development of the visual system (Tiriac, Smith, &
222 Feller, 2018). Thus, we hypothesised that visual experience may alter the network
223 properties of dLGN neurons, allowing CTAs to enter the dLGN. To test this possibility,
224 we maintained control and Th^{Kir} mice in a dark rearing (DR) environment from P5 until
225 P15 and we then analysed the CTA innervation of the dLGN (**Figure 6C**). We did not
226 find major modifications in CTA innervation at P15 in control animals subjected to DR
227 (**Figure 6D and 6E**). However, in contrast to the Th^{Kir} mice, there was a significant
228 reduction in CTA invasion of the dLGN in DR Th^{Kir} mice after eye opening (**Figure 6D**
229 **and 6E**). Together these results demonstrate that early visual experience is necessary
230 for the plastic recovery of CTA invasion of the dLGN that occurs in juvenile Th^{Kir} mice.
231
232
233 **Discussion**
234 Here we describe a novel aspect in the coordination of afferent connectivity to the
235 dLGN by intrinsic thalamic spontaneous activity. Using a model in which spontaneous
236 dLGN activity is perturbed, we show that the timing of CTA entry into this structure
237 depends on this thalamic activity. In a scenario of impaired thalamic spontaneous
238 activity, CTA invasion of the dLGN is severely delayed. In addition, the lack of calcium
239 waves in the dLGN leads to a decrease in its size and a concomitant increase in cell
240 death, as occurs after embBE or in Math5 mutant mice where retinal input is absent
241 from embryonic stages (El-Danaf et al., 2015; Moreno-Juan et al., 2017). Hence, in
242 addition to the trophic factors produced by retinal innervation, spontaneous thalamic
243 activity may directly regulate dLGN neuronal survival, as in the developing cortex
244 (Blanquie et al., 2017; Luhmann & Khazipov, 2018). However, it is also possible that

245 the effect on cell death is indirect and due to the lack of a proper corticogeniculate
246 innervation, although this will require further study. While CTAs invade the dLGN after
247 RTAs, it was suggested that CTAs regulate the initial targeting of the visual thalamus
248 by the retina. In transgenic mice in which the V1 was eliminated and where CTAs
249 therefore fail to develop, some RGCs did not project to the dLGN (Diao et al., 2018;
250 Shanks et al., 2016). Moreover, when the activity of L6 neurons was silenced in the V1,
251 functional modifications were apparent in visually-evoked activity in the thalamus
252 (Denman & Contreras, 2015). Despite these findings, our work on the Th^{Kir} mice in
253 which CTAs are absent in the dLGN and RTAs normally innervate this nucleus suggest
254 the retinothalamic afferents from the CTAs initial develop following an independent
255 programme.

256 Retinal waves are transmitted to the dLGN and the superior colliculus, and this
257 transmission is crucial for the correct development of visual topographic maps
258 (Ackman, Burbridge, & Crair, 2012; Colonnese & Khazipov, 2010; Mooney, Penn,
259 Gallego, & Shatz, 1996; Siegel, Heimel, Peters, & Lohmann, 2012). During prenatal
260 development, type I retinal waves coexist with the other patterns of spontaneous activity
261 in the thalamus. Although the role of type I retinal waves in visual system development
262 remains poorly understood, here we demonstrate that embryonic ablation of the retinal
263 input, before the retinal axons reach the dLGN, modulates thalamic wave activity. We
264 found that the frequency of thalamic calcium waves augments in the dLGN of embBE
265 mice, which leads to a premature invasion of the dLGN by CTAs. Although the
266 functional synapses between CTAs and dLGN neurons are established during the
267 second postnatal week (Seabrook et al., 2013; Bickford et al., 2010), vGlut1 is already
268 present in the terminals of the CTAs that invade the dLGN of embBE mice at P1. This
269 transporter has previously been associated with functional excitatory transmission

270 (Koch et al., 2011; Marcucci, Zou, & Firestein, 2009; Nakamura, Hioki, Fujiyama, &
271 Kaneko, 2005; Sherry, Wang, Bates, & Frishman, 2003; Wilson et al., 2005). Thus, it is
272 possible that eliminating retinal input accelerates corticogeniculate maturation in the
273 dLGN.

274 Our data from Th^{Kir} mice indicate that spontaneous thalamic activity is crucial
275 for the timely invasion of the dLGN by CTAs but also, they helped us unravel the
276 hierarchical organization of RTAs, CTAs and thalamic spontaneous activity. When
277 retinal input is eliminated in Th^{Kir} mice the lack of CTAs in the dLGN was completely
278 rescued, as not only the absence of thalamic waves but also, the presence of RTAs in
279 Th^{Kir} mice prevented the entry of CTAs into the dLGN. As such, it would appear that
280 RTAs and CTAs compete for dLGN innervation, with RTAs arriving first, and that
281 spontaneous thalamic activity represents a permissive phenomenon in this context.

282 The analysis of CTAs in postnatal Th^{Kir} mice shows that the delay in CTA
283 invasion of the dLGN is reversed at eye-opening, when visually evoked activity
284 commences and spontaneous retinal waves subside (Demas, Eglen, & Wong, 2003;
285 Huberman et al., 2008). At this stage, CTAs innervate the dLGN despite the disturbed
286 thalamic activity, suggesting that visual evoked inputs are sufficient to drive CTA
287 innervation of the dLGN. Indeed, visual evoked activity is necessary for this recovery as
288 CTAs did not fully recover in DR Th^{Kir} mice.

289 In summary, our data suggest patterned spontaneous activity in the perinatal
290 thalamus provides a fundamental signal that regulates the timing of CTA invasion of the
291 dLGN, indicating that the thalamus is as a key structure in the development of visual
292 circuits. Furthermore, these results also suggest the existence of an experience-
293 dependent mechanism that helps to recover from early defects in circuits within the
294 visual system.

Acknowledgments

The authors are grateful to L.M. Rodríguez, B. Andrés and R. Susín for their excellent technical support; to T. Theil and A. Campagnoni for providing the *Golli-tau-eGfp* mouse line; and to members of G. López-Bendito's laboratory for stimulating discussions. Funding: this work was supported by grants from the European Research Council (ERC-2014-CoG-647012) and the Spanish Ministry of Science, Innovation and Universities (PGC2018/096631-B-I00, BFU2015-64432-R and Severo Ochoa Grant SEV-2017-0723).

Author Contributions

V.M-J. and G.L-B. conceived the idea and designed the experiments. V.M-J. conducted the experiments and analyzed the calcium imaging data, corticothalamic innervation, cell death, CTB tracing, embryonic enucleations and dark-reared experiments. L.P-S performed the *in vivo* recordings in the Th^{Kir} mice, F.J.M generated the Matlab codes and F.J.M and L.P-S analyzed this data. A.H-N performed the lentiviral injections in Th^{Kir} mice. G.L-B. acquired the funding; V.M-J, F.J.M, M.V and G.L-B. wrote the paper.

Declaration of Interests

The authors have no competing interests to declare

318 **References**

319 Ackman, J. B., Burbridge, T. J., & Crair, M. C. (2012). Retinal waves coordinate
320 patterned activity throughout the developing visual system. *Nature*, *490*(7419),
321 219–225. http://doi.org/10.1038/nature11529

322 Ahern, T. H., Krug, S., Carr, A. V., Murray, E. K., Fitzpatrick, E., Bengston, L., et al.
323 (2013). Cell death atlas of the postnatal mouse ventral forebrain and hypothalamus:
324 effects of age and sex. *The Journal of Comparative Neurology*, *521*(11), 2551–
325 2569. http://doi.org/10.1002/cne.23298

326 Antón-Bolaños, N., Sempere-Ferràndez, A., Guillamón-Vivancos, T., Martini, F. J.,
327 Pérez-Saiz, L., Gezelius, H., et al. (2019). Prenatal activity from thalamic neurons
328 governs the emergence of functional cortical maps in mice. *Science (New York,*
329 *N.Y.)*, *364*(6444), 987–990. http://doi.org/10.1126/science.aav7617

330 Bickford, M. E., Slusarczyk, A., Dilger, E. K., Krahe, T. E., Kucuk, C., & Guido, W.
331 (2009). Synaptic development of the mouse dorsal lateral geniculate nucleus. *The*
332 *Journal of Comparative Neurology*, *518*(5), 622–635.
333 http://doi.org/10.1002/cne.22223

334 Blanquie, O., Yang, J.-W., Kilb, W., Sharopov, S., Sinning, A., & Luhmann, H. J.
335 (2017). Electrical activity controls area-specific expression of neuronal apoptosis in
336 the mouse developing cerebral cortex. *eLife*, *6*. http://doi.org/10.7554/eLife.27696

337 Brooks, J. M., Su, J., Levy, C., Wang, J. S., Seabrook, T. A., Guido, W., & Fox, M. A.
338 (2013). A molecular mechanism regulating the timing of corticogeniculate
339 innervation. *Cell Reports*, *5*(3), 573–581.
340 http://doi.org/10.1016/j.celrep.2013.09.041

341 Castillo-Paterna, M., Moreno-Juan, V., Filipchuk, A., Rodríguez-Malmierca, L., Susín,
342 R., & López-Bendito, G. (2015). DCC functions as an accelerator of

thalamocortical axonal growth downstream of spontaneous thalamic activity. *EMBO Reports*, *16*(7), 851–862. http://doi.org/10.15252/embr.201439882

Chen, L., Guo, Q., & Li, J. Y. H. (2009). Transcription factor Gbx2 acts cell-nonautonomously to regulate the formation of lineage-restriction boundaries of the thalamus. *Development*, *136*(8), 1317–1326. http://doi.org/10.1242/dev.030510

Colonnese, M. T., & Khazipov, R. (2010). "Slow activity transients" in infant rat visual cortex: a spreading synchronous oscillation patterned by retinal waves. *Journal of Neuroscience*, *30*(12), 4325–4337. http://doi.org/10.1523/JNEUROSCI.4995-09.2010

Demas, J., Eglen, S. J., & Wong, R. O. L. (2003). Developmental loss of synchronous spontaneous activity in the mouse retina is independent of visual experience. *The Journal of Neuroscience : the Official Journal of the Society for Neuroscience*, *23*(7), 2851–2860. http://doi.org/10.1523/JNEUROSCI.23-07-02851.2003

Denman, D. J., & Contreras, D. (2015). Complex Effects on In Vivo Visual Responses by Specific Projections from Mouse Cortical Layer 6 to Dorsal Lateral Geniculate Nucleus. *Journal of Neuroscience*, *35*(25), 9265–9280. http://doi.org/10.1523/JNEUROSCI.0027-15.2015

Diao, Y., Cui, L., Chen, Y., Burbridge, T. J., Han, W., Wirth, B., et al. (2018). Reciprocal Connections Between Cortex and Thalamus Contribute to Retinal Axon Targeting to Dorsal Lateral Geniculate Nucleus. *Cerebral Cortex*, *28*(4), 1168–1182. http://doi.org/10.1093/cercor/bhx028

Drager, U. C., & Hubel, D. H. (1975). Physiology of visual cells in mouse superior colliculus and correlation with somatosensory and auditory input. *Nature*, *253*(5488), 203–204. http://doi.org/10.1038/253203a0

El-Danaf, R. N., Krahe, T. E., Dilger, E. K., Bickford, M. E., Fox, M. A., & Guido, W. (2015). Developmental remodeling of relay cells in the dorsal lateral geniculate nucleus in the absence of retinal input. *Neural Development*, *10*(1), 19–17. http://doi.org/10.1186/s13064-015-0046-6

Erişir, A., Bickford, M. E., Van Horn, S. C., & Sherman, S. M. (1997). Relative numbers of cortical and brainstem inputs to the lateral geniculate nucleus. *Proceedings of the National Academy of Sciences of the United States of America*, *94*(4), 1517–1520. http://doi.org/10.1073/pnas.94.4.1517

Fox, M. A., & Guido, W. (2011). Shedding light on class-specific wiring: development of intrinsically photosensitive retinal ganglion cell circuitry. *Molecular Neurobiology*, *44*(3), 321–329. http://doi.org/10.1007/s12035-011-8199-8

Godement, P., Salaün, J., & Imbert, M. (1984a). Prenatal and postnatal development of retinogeniculate and retinocollicular projections in the mouse. *The Journal of Comparative Neurology*, *230*(4), 552–575. http://doi.org/10.1002/cne.902300406

Godement, P., Salaün, J., & Imbert, M. (1984b). Prenatal and postnatal development of retinogeniculate and retinocollicular projections in the mouse. *The Journal of Comparative Neurology*, *230*(4), 552–575. http://doi.org/10.1002/cne.902300406

Godwin, D. W., Van Horn, S. C., Eriir, A., Sesma, M., Romano, C., & Sherman, S. M. (1996). Ultrastructural localization suggests that retinal and cortical inputs access different metabotropic glutamate receptors in the lateral geniculate nucleus. *Journal of Neuroscience*, *16*(24), 8181–8192. http://doi.org/10.1523/JNEUROSCI.16-24-08181.1996

Grant, E., Hoerder-Suabedissen, A., & Molnár, Z. (2016). The Regulation of Corticofugal Fiber Targeting by Retinal Inputs. *Cerebral Cortex*, *26*(3), 1336–1348. http://doi.org/10.1093/cercor/bhv315

392 Guido, W. (2018). Development, form, and function of the mouse visual thalamus.
393 *Journal of Neurophysiology*, *120*(1), 211–225. http://doi.org/10.1152/jn.00651.2017
394 Hensch, T. K. (2005). Critical period plasticity in local cortical circuits. *Nature Reviews*
395 *Neuroscience*, *6*(11), 877–888. http://doi.org/10.1038/nrn1787
396 Hofer, S. B., Mrsic-Flogel, T. D., Bonhoeffer, T., & Hübener, M. (2009). Experience
397 leaves a lasting structural trace in cortical circuits. *Nature*, *457*(7227), 313–317.
398 http://doi.org/10.1038/nature07487
399 Hooks, B. M., & Chen, C. (2006). Distinct roles for spontaneous and visual activity in
400 remodeling of the retinogeniculate synapse. *Neuron*, *52*(2), 281–291.
401 http://doi.org/10.1016/j.neuron.2006.07.007
402 Huberman, A. D., Manu, M., Koch, S. M., Susman, M. W., Lutz, A. B., Ullian, E. M.,
403 et al. (2008). Architecture and activity-mediated refinement of axonal projections
404 from a mosaic of genetically identified retinal ganglion cells. *Neuron*, *59*(3), 425–
405 438. http://doi.org/10.1016/j.neuron.2008.07.018
406 Jacobs, E. C., Campagnoni, C., Kampf, K., Reyes, S. D., Kalra, V., Handley, V., et al.
407 (2007). Visualization of corticofugal projections during early cortical development
408 in a tau-GFP-transgenic mouse. *The European Journal of Neuroscience*, *25*(1), 17–
409 30. http://doi.org/10.1111/j.1460-9568.2006.05258.x
410 Jurgens, C. W. D., Bell, K. A., McQuiston, A. R., & Guido, W. (2012). Optogenetic
411 stimulation of the corticothalamic pathway affects relay cells and GABAergic
412 neurons differently in the mouse visual thalamus. *PloS One*, *7*(9), e45717.
413 http://doi.org/10.1371/journal.pone.0045717
414 Koch, S. M., Cruz, Dela, C. G., Hnasko, T. S., Edwards, R. H., Huberman, A. D., &
415 Ullian, E. M. (2011). Pathway-specific genetic attenuation of glutamate release

alters select features of competition-based visual circuit refinement. *Neuron*, *71*(2), 235–242. http://doi.org/10.1016/j.neuron.2011.05.045

Lossi, L., Castagna, C., & Merighi, A. (2015). Neuronal cell death: an overview of its different forms in central and peripheral neurons. *Methods in Molecular Biology (Clifton, N.J.)*, *1254*, 1–18. http://doi.org/10.1007/978-1-4939-2152-2_1

Luhmann, H. J., & Khazipov, R. (2018). Neuronal activity patterns in the developing barrel cortex. *Neuroscience*, *368*, 256–267. http://doi.org/10.1016/j.neuroscience.2017.05.025

Marcucci, F., Zou, D.-J., & Firestein, S. (2009). Sequential onset of presynaptic molecules during olfactory sensory neuron maturation. *The Journal of Comparative Neurology*, *516*(3), 187–198. http://doi.org/10.1002/cne.22094

McCormick, D. A., & Krosigk, von, M. (1992). Corticothalamic activation modulates thalamic firing through glutamate "metabotropic" receptors. *Proceedings of the National Academy of Sciences of the United States of America*, *89*(7), 2774–2778. http://doi.org/10.1073/pnas.89.7.2774

Mire, E., Mezzera, C., Leyva-Díaz, E., Paternain, A. V., Squarzoni, P., Bluy, L., et al. (2012). Spontaneous activity regulates Robo1 transcription to mediate a switch in thalamocortical axon growth. *Nature Neuroscience*, *15*(8), 1134–1143. http://doi.org/10.1038/nn.3160

Mooney, R., Penn, A. A., Gallego, R., & Shatz, C. J. (1996). Thalamic relay of spontaneous retinal activity prior to vision. *Neuron*, *17*(5), 863–874. http://doi.org/10.1016/s0896-6273(00)80218-4

Moreno-Juan, V., Filipchuk, A., Antón-Bolaños, N., Mezzera, C., Gezelius, H., Andrés, B., et al. (2017). Prenatal thalamic waves regulate cortical area size prior to sensory

processing. *Nature Communications*, *8*(1), 14172–14. http://doi.org/10.1038/ncomms14172

Nakamura, K., Hioki, H., Fujiyama, F., & Kaneko, T. (2005). Postnatal changes of vesicular glutamate transporter (VGluT)1 and VGluT2 immunoreactivities and their colocalization in the mouse forebrain. *The Journal of Comparative Neurology*, *492*(3), 263–288. http://doi.org/10.1002/cne.20705

Pecka, M., Han, Y., Sader, E., & Mrsic-Flogel, T. D. (2014). Experience-dependent specialization of receptive field surround for selective coding of natural scenes. *Neuron*, *84*(2), 457–469. http://doi.org/10.1016/j.neuron.2014.09.010

Piñon, M. C., Jethwa, A., Jacobs, E., Campagnoni, A., & Molnár, Z. (2009). Dynamic integration of subplate neurons into the cortical barrel field circuitry during postnatal development in the Golli-tau-eGFP (GTE) mouse. *The Journal of Physiology*, *587*(Pt 9), 1903–1915. http://doi.org/10.1113/jphysiol.2008.167767

Seabrook, T. A., El-Danaf, R. N., Krahe, T. E., Fox, M. A., & Guido, W. (2013). Retinal input regulates the timing of corticogeniculate innervation. *The Journal of Neuroscience : the Official Journal of the Society for Neuroscience*, *33*(24), 10085–10097. http://doi.org/10.1523/JNEUROSCI.5271-12.2013

Shanks, J. A., Ito, S., Schaevitz, L., Yamada, J., Chen, B., Litke, A., & Feldheim, D. A. (2016). Corticothalamic Axons Are Essential for Retinal Ganglion Cell Axon Targeting to the Mouse Dorsal Lateral Geniculate Nucleus. *The Journal of Neuroscience : the Official Journal of the Society for Neuroscience*, *36*(19), 5252–5263. http://doi.org/10.1523/JNEUROSCI.4599-15.2016

Shatz, C. J., & Rakic, P. (1981a). The genesis of efferent connections from the visual cortex of the fetal rhesus monkey. *The Journal of Comparative Neurology*, *196*(2), 287–307. http://doi.org/10.1002/cne.901960208

Shatz, C. J., & Rakic, P. (1981b). The genesis of efferent connections from the visual cortex of the fetal rhesus monkey. *The Journal of Comparative Neurology*, *196*(2), 287–307. http://doi.org/10.1002/cne.901960208

Sherry, D. M., Wang, M. M., Bates, J., & Frishman, L. J. (2003). Expression of vesicular glutamate transporter 1 in the mouse retina reveals temporal ordering in development of rod vs. cone and ON vs. OFF circuits. *The Journal of Comparative Neurology*, *465*(4), 480–498. http://doi.org/10.1002/cne.10838

Siegel, F., Heimel, J. A., Peters, J., & Lohmann, C. (2012). Peripheral and central inputs shape network dynamics in the developing visual cortex in vivo. *Current Biology : CB*, *22*(3), 253–258. http://doi.org/10.1016/j.cub.2011.12.026

Thompson, A. D., Picard, N., Min, L., Fagiolini, M., & Chen, C. (2016). Cortical Feedback Regulates Feedforward Retinogeniculate Refinement. *Neuron*, *91*(5), 1021–1033. http://doi.org/10.1016/j.neuron.2016.07.040

Thompson, A., Gribizis, A., Chen, C., & Crair, M. C. (2017). Activity-dependent development of visual receptive fields. *Current Opinion in Neurobiology*, *42*, 136–143. http://doi.org/10.1016/j.conb.2016.12.007

Tiriac, A., Smith, B. E., & Feller, M. B. (2018). Light Prior to Eye Opening Promotes Retinal Waves and Eye-Specific Segregation. *Neuron*, *100*(5), 1059–1065.e4. http://doi.org/10.1016/j.neuron.2018.10.011

Varoqui, H., Schäfer, M. K. H., Zhu, H., Weihe, E., & Erickson, J. D. (2002). Identification of the differentiation-associated Na+/PI transporter as a novel vesicular glutamate transporter expressed in a distinct set of glutamatergic synapses. *The Journal of Neuroscience : the Official Journal of the Society for Neuroscience*, *22*(1), 142–155. http://doi.org/10.1523/JNEUROSCI.22-01-00142.2002

Wilson, N. R., Kang, J., Hueske, E. V., Leung, T., Varoqui, H., Murnick, J. G., et al. (2005). Presynaptic regulation of quantal size by the vesicular glutamate transporter VGLUT1. *Journal of Neuroscience*, *25*(26), 6221–6234. http://doi.org/10.1523/JNEUROSCI.3003-04.2005

Zipursky, S. L., & Sanes, J. R. (2010). Chemoaffinity revisited: dscams, protocadherins, and neural circuit assembly. *Cell*, *143*(3), 343–353. http://doi.org/10.1016/j.cell.2010.10.009

498 **Main Figures**

499

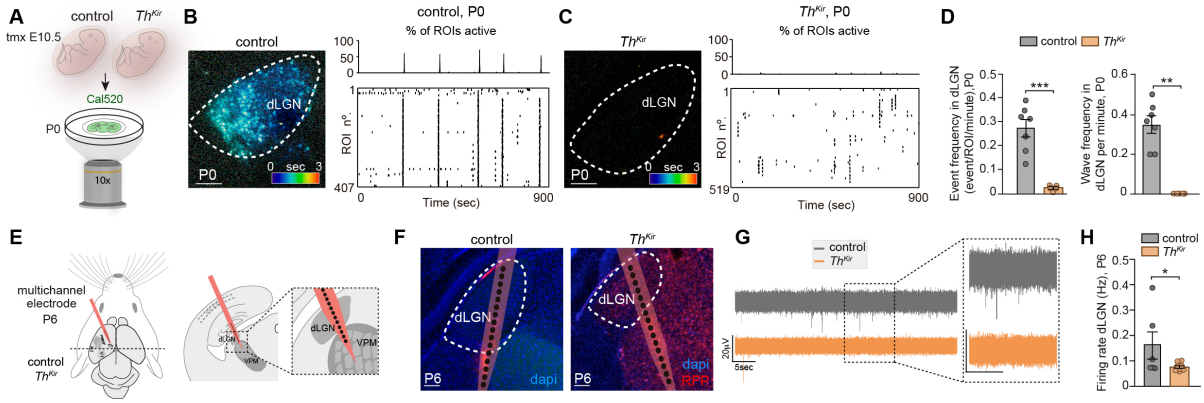

500

501

502 **Figure 1. Overexpression of Kir2.1 gene in the dLGN disrupts the patterns of**

503 **spontaneous activity.** (A) Scheme of the experimental design used for calcium imaging

504 of *ex vivo* slices from control and *Th*^{Kir} mice at P0. (B) *Left*, maximal projection of an *ex*

505 *vivo* thalamic spontaneous calcium wave in the dLGN of a control mouse at P0. *Right*,

506 quantification of the relative active Region Of Interest (ROIs) in the dLGN over a 15

507 minute recording (top), and the corresponding raster plot of the active ROIs per frame

508 (bottom). (C) *Left*, maximal projection of *ex vivo* thalamic spontaneous calcium activity

509 in the dLGN of *Th*^{Kir} mouse at P0. *Right*, quantification of the proportion of active ROIs

510 in the dLGN over 15 minutes recording (top) and the corresponding raster plot of active

511 ROIs per frame (bottom). (D) *Left,* graph showing the mean event frequency per ROI

512 per minute in the dLGN of control and *Th*^{Kir} mice. *Right,* graph showing the mean

513 frequency of the waves in the dLGN of control and *Th*^{Kir} mice at P0 (control $n = 7$, *Th*^{Kir}

514 $n = 5$). (E) Scheme of the experimental design used for the *in vivo* recording of

515 spontaneous activity in control and *Th*^{Kir} mice at P6. (F) Coronal sections of control and

516 *Th*^{Kir} mice revealing the position of the recording electrodes in the dLGN. Red

517 fluorescence corresponds to the mCherry fused to the Kir2.1 gene (labelled by RFP

518 immunostaining). (G) Sample traces that illustrate the spiking activity in control and

519 Th^{Kir} mice at P6. (H) Quantification of the firing rate in the dLGN at P6 (control $n = 6$,

520 Th^{Kir} $n = 8$). Graphs represent the mean ± SEM, each dot corresponding to a single

521 value: *P<0.05, **P<0.01, ***P<0.001. Scale bars, 100 μm.

522

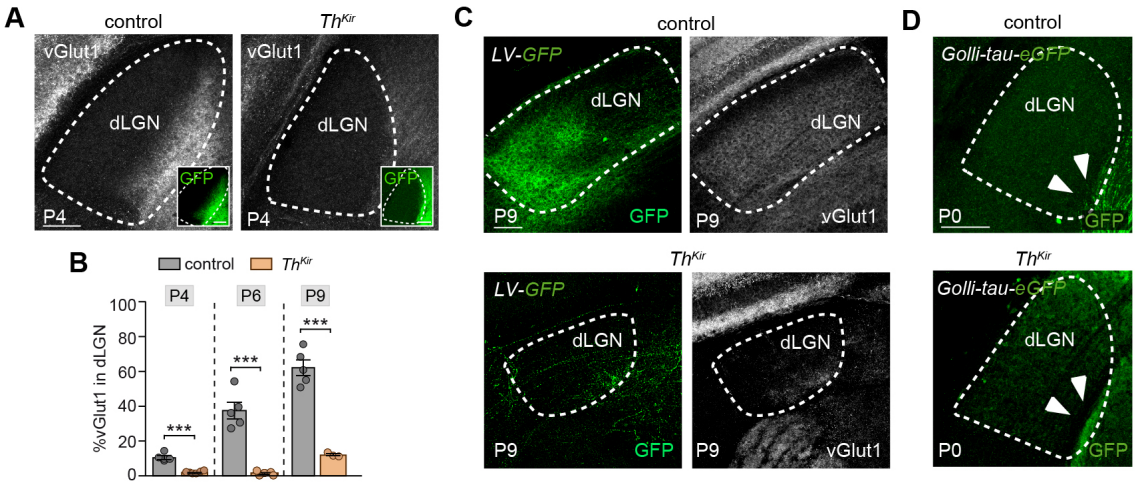

Figure 2. Correct spontaneous activity in the dLGN is necessary for the invasion of CTAs. (A) Coronal sections of *Golli-tau-eGfp* in control and *Th*^{Kir} mice at P4 showing the expression of vGlut1 in the dLGN. Insets show GFP immunostaining. (B) Quantification of the relative dLGN area occupied by vGlut1 in control and *Th*^{Kir} mice at different postnatal stages (P4 control $n = 5$, *Th*^{Kir} $n = 5$; P6 control $n = 5$, *Th*^{Kir} $n = 5$; P9 control $n = 5$, *Th*^{Kir} $n = 3$). (C) Coronal sections of control and *Th*^{Kir} mice at P9 showing vGlut1 and Gfp expression in CTAs. A lentivirus expressing *Gfp* was injected into V1. (D) Coronal sections of *Golli-tau-eGfp* control and *Th*^{Kir} mice at P0 showing the expression of Gfp in CTAs (see arrowheads) in the dLGN (control $n = 3$, *Th*^{Kir} $n = 6$). Graphs represent the mean ± SEM and each dot correspond to a single value: *P<0.05, **P<0.01, ***P<0.001. Scale bars, 100 µm.

537

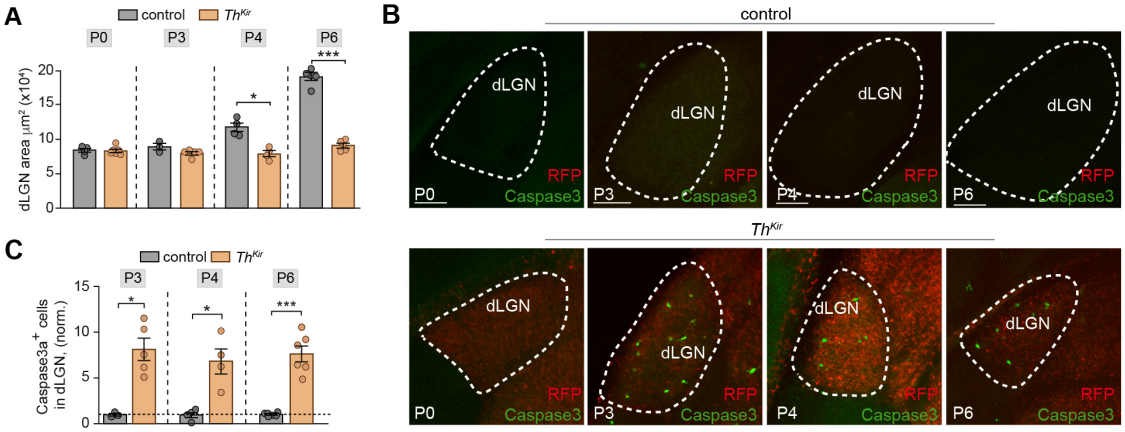

538

539

540 **Figure 3. Significant increase in cell death in the dLGN of *Th^Kir^* mice.** (A)

541 Quantification of the dLGN area in controls and *Th^Kir^* mice (P0 control $n = 4$, *Th^Kir^* $n =$

542 6; P3 control $n = 3$, *Th^Kir^* $n = 5$; P4 control $n = 4$, *Th^Kir^* $n = 4$; P6 control $n = 5$, *Th^Kir^* $n =$

543 5). (B) Coronal sections of control and *Th^Kir^* mice showing caspase3a positive cells and

544 mCherry fused to Kir2.1 (labelled by RFP immunostaining) at P0, P3, P4 and P6. Note

545 that no caspase3a positive cells were found in P0 *Th^Kir^* mice. (C) Quantification of

546 caspase3a positive cells in the dLGN of control and *Th^Kir^* mice at P3, P4 and P6 (P3

547 control $n = 3$, *Th^Kir^* $n = 5$; P4 control $n = 4$, *Th^Kir^* $n = 4$; P6 control $n = 5$, *Th^Kir^* $n = 5$).

548 The graphs represent the mean ± SEM and each dot corresponds to a single value:

549 *P<0.05, **P<0.01, ***P<0.001. Scale bars, 100 µm.

550

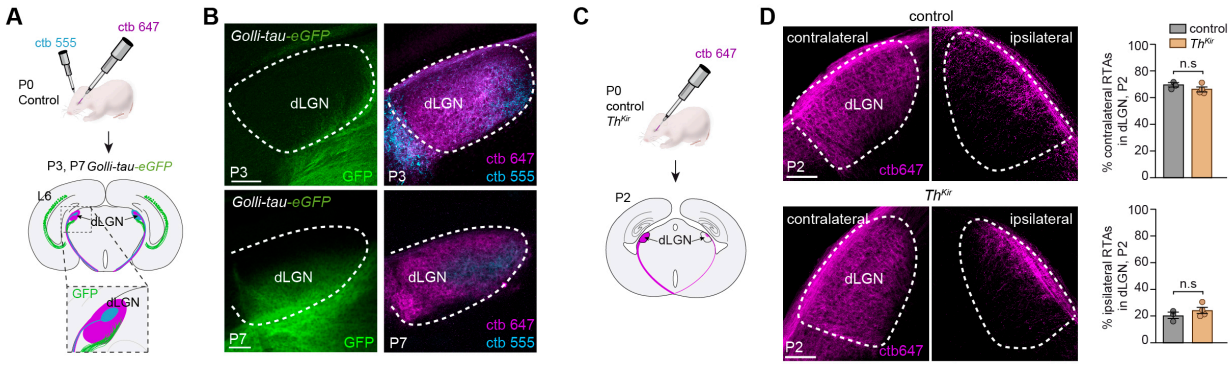

Figure 4. RTAs correctly invade the dLGN of *Th^{Kir}* mice. (A) Scheme of the experimental design used to label CTAs and RTAs in control P3 and P7 mice. Injections of CTB-555 and CTB-647 were performed in each eye of *Golli-tau-eGFP* mice at P0, and they were analysed at P3 and P7 by immunostaining for GFP. (B) Coronal sections of *Golli-tau-eGfp* mice at P3 and P7 showing GFP expression in CTAs (green), and the contralateral (CTB-647) and ipsilateral RTAs (CTB-555). (C) Scheme of the experimental design used to label RTAs in control and *Th^{Kir}* mice at P2. Injection of CTB-647 was performed in one eye in control and *Th^{Kir}* mice at P0 and analysed at P2. (D) *Left*: Coronal sections showing CTB-647 labelling in the contralateral and ipsilateral retinal axons in the dLGN of control and *Th^{Kir}* mice at P2. *Right*: Quantification of the percentage of contralateral and ipsilateral RTAs in the dLGN at P2 (control $n = 3$, *Th^{Kir}* $n = 4$). The graphs represent the mean ± SEM and each dot corresponds to a single value. Scale bars, 100 µm.

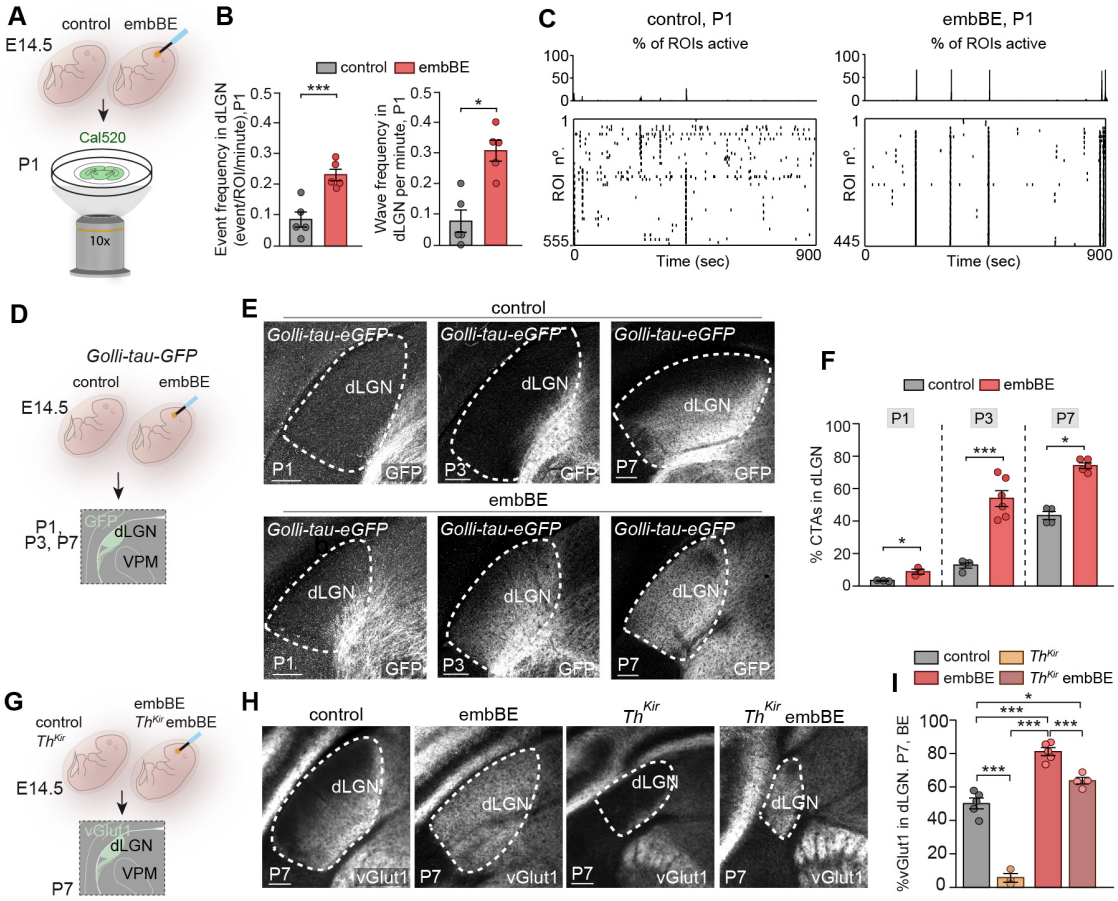

Figure 5. Innervation of the dLGN by CTAs is dictated by RTAs and thalamic spontaneous activity plays a permissive role. (A) Scheme of the experimental design used for *ex vivo* calcium imaging of the dLGN in control and embBE mice at P1. (B) *Left*, quantification of the event frequency of spontaneous calcium activity in the dLGN in controls and embBE mice at P1. *Right*, quantification of the frequency of thalamic calcium waves in the dLGN of control and embBE mice at P1 (control $n = 5$, embBE $n = 5$). (C) *Upper panel*, quantification of the percentage of active ROIs over 15 minutes recordings in control and embBE mice. *Lower panel*, raster plot of the number of active ROIs per frame. (D) Scheme of the experimental design used to reveal L6 cortical axons in the *Golli-tau-Gfp* mice that were embryonically enucleated at E14.5. (E) Coronal sections of control and embBE mice showing GFP immunostaining in CTAs at P1, P3

579 and P7. (F) Quantification of the percentage of the dLGN area occupied by GFP-
580 positive axons (P1: control n = 3, embBE n = 3; P3: control n = 4, embBE n = 6; P7
581 control n = 5, embBE n = 5). (G) Scheme of the experimental design used to reveal
582 CTAs in embBE Th^{Kir} mice. Tamoxifen was administered at E10.5 and embBE was
583 performed at E14.5 in control and Th^{Kir} mice. (H) Coronal sections showing vGlut1
584 immunostaining in the dLGN in control (n= 5), Th^{Kir} (n= 3), embBE (n= 5), and embBE
585 Th^{Kir} (n= 4) mice at P7. (I) Quantification of the relative vGlut1 immunostaining in the
586 dLGN of control, Th^{Kir}, embBE and embBE Th^{Kir} mice at P7. Note that CTAs invade
587 the dLGN of the Th^{Kir} embBE mice. Graphs represent the mean ± SEM and each dot
588 correspond to a single value: *P<0.05, **P<0.01, ***P<0.001. Scale bars, 100 µm.

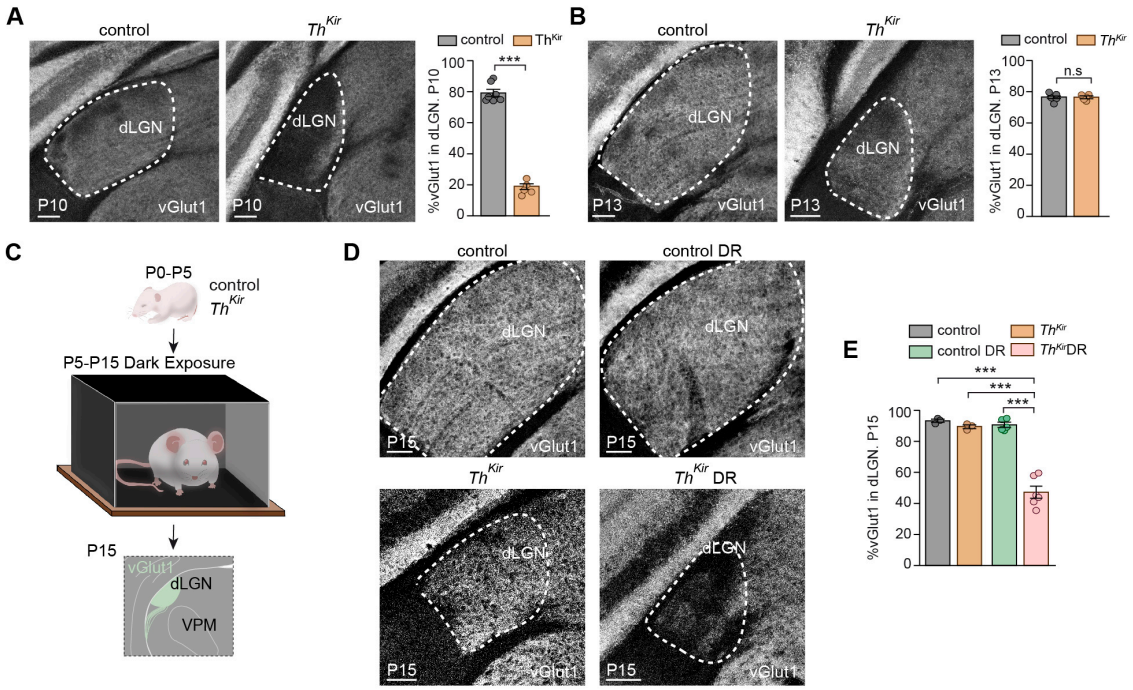

589

590 **Figure 6. Eye-opening recues the entry of CTAs in *Th^Kir* mice.** (A) *Left:* Coronal
591 sections from P10 control and *Th^Kir* mice showing vGlut1 immunostaining in the dLGN
592 at P10, before eye opening. *Right:* Quantification of the relative dLGN area occupied by
593 vGlut1 labelling at P10 (control $n = 7$, *Th^Kir* $n = 6$). (B) *Left:* Coronal sections from P13
594 control and *Th^Kir* mice showing vGlut1 immunostaining at P13, after eye opening.
595 *Right:* Quantification of the relative dLGN area occupied by vGlut1 labelling at P13
596 (control $n = 5$, *Th^Kir* $n = 5$). (C) Scheme of the experimental design used for the dark
597 rearing (DR) experiments. Control and *Th^Kir* mice were place in a dark room from P5 to
598 P15. (D) Coronal sections showing the vGlut1 immunostaining in the dLGN of control,
599 control DR, *Th^Kir* and *Th^Kir* DR mice. (E) Quantification of the relative dLGN area
600 occupied by vGlut1 labelling in these four conditions: Control ($n = 3$), *Th^Kir* ($n = 3$),
601 control DR ($n = 5$), and *Th^Kir* DR ($n = 6$). The graphs represent the mean ± SEM and
602 each dot corresponds to a single value: *P<0.05, **P<0.01, ***P<0.001. Scale bars,
603 100 µm.

604

605 **Supplementary Figures**

606

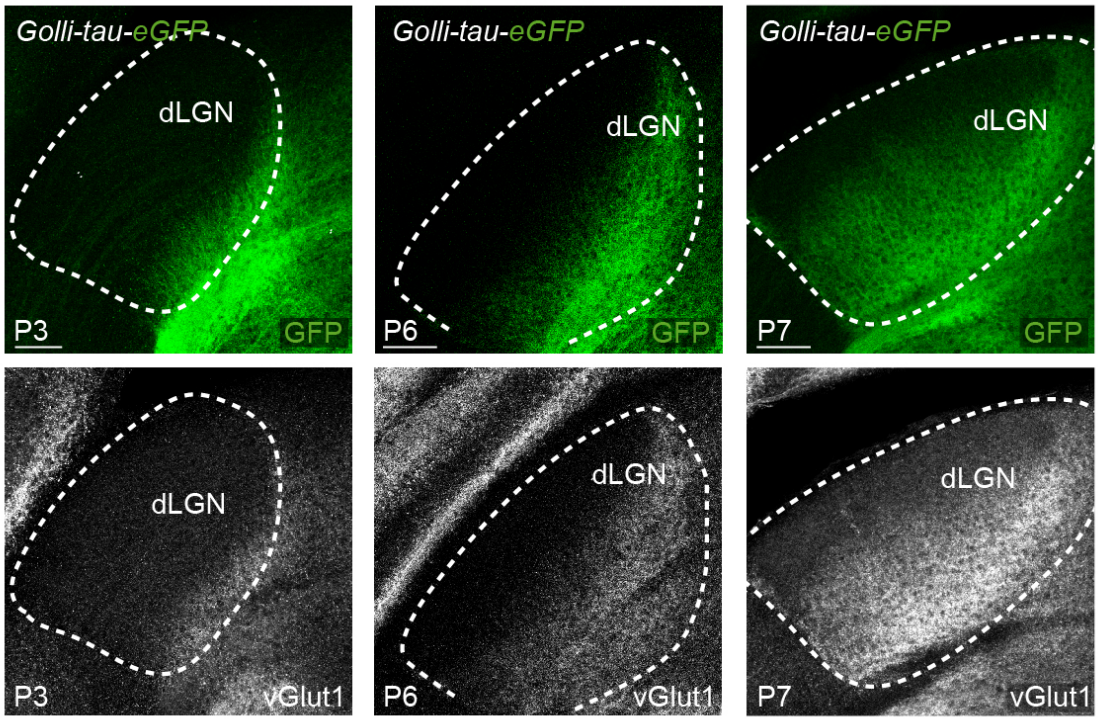

607

608 **Figure S1. Distribution of CTAs and vGlut1 expression in the dLGN**. Coronal

609 sections showing CTAs labelled by *Golli-tau-eGfp* and immunostaining against vGlut1

610 in the dLGN of P3 (n = 6), P6 (n = 3) and P7 (n = 3) mice. CTAs start to invade the

611 dLGN around P3. Scale bars, 100 μm.

612

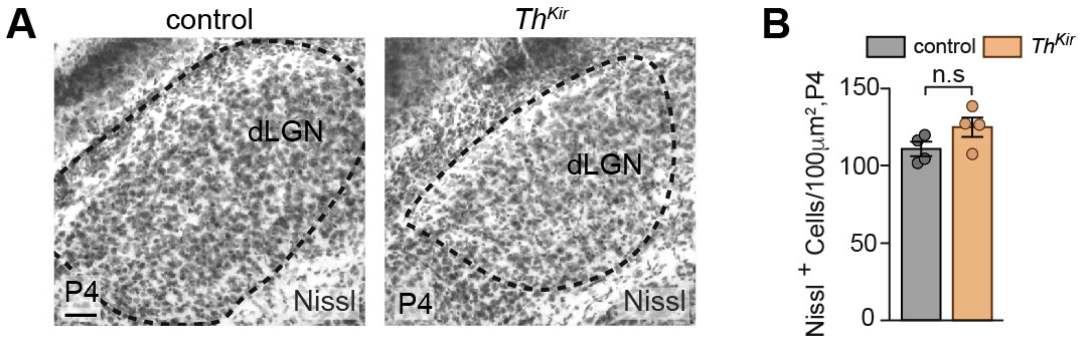

Figure S2. The density of dLGN cells remains normal in *Th^{Kir}* mice. (A) Coronal sections showing Nissl staining of control and *Th^{Kir}* mice at P4. (B) Quantification of the data shown in A. No significant changes in cell density were observed between the control (n = 4) and *Th^{Kir}* mice (n = 4). The graph represents the mean ± SEM and each dot correspond to a single value: *P<0.05, **P<0.01, ***P<0.001. Scale bars, 100 μm.

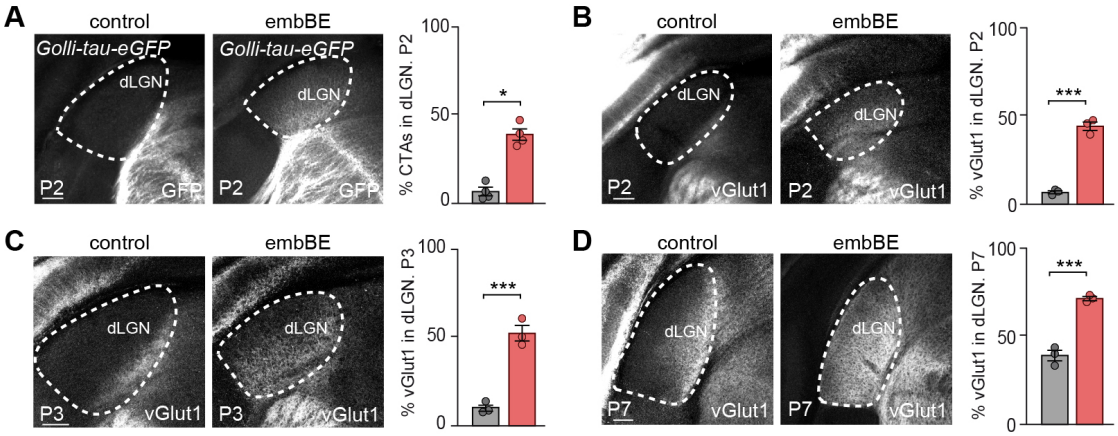

Figure S3. Early CTA invasion of the dLGN in embBE mice. (A) *Left*, Coronal sections of the dLGN showing CTAs labelled with GFP in control and embBE *Golli-tau-eGfp* mice at P2. *Right*, Quantification of the data shown on the left (control $n = 4$, embBE $n = 4$). (B, C and D) *Left*, Coronal sections of the dLGN showing vGlut1 immunostaining in control and embBE mice at P2 (control $n = 3$, embBE $n = 3$), P3 (control $n = 3$, embBE $n = 3$) and P7 (control $n = 3$, embBE $n = 3$). *Right*, Quantification of the data shown in the images on the left. Note that in all embBE mice a higher percentage of CTAs invaded the dLGN. The graphs represent the mean ± SEM and each dot corresponds to a single value: *P<0.05, **P<0.01, ***P<0.001. Scale bars, 100 μm.

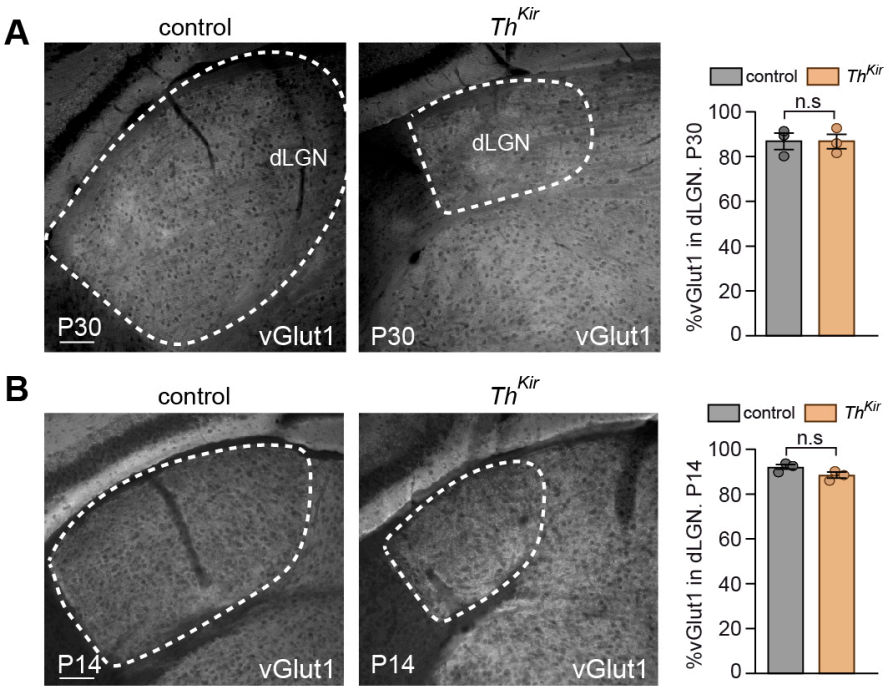

Figure S4. Normal pattern of dLGN invasion by CTAs after eye opening. (A) *Left*, Coronal sections showing vGlut1 immunostaining in control and Th^{Kir} mice at P30. *Right*, Quantification of the dLGN area occupied by vGlut1 expression at P30 (control *n*= 3, Th^{Kir} *n*= 3). No significant differences were found between both conditions. (B) *Left,* Coronal sections showing vGlut1 immunostaining in control and Th^{Kir} mice at P14. *Right*, Quantification of the dLGN area occupied by vGlut1 expression at P14 (control *n*= 3, Th^{Kir} *n*= 3). No significant differences were found between both conditions. The graphs represent the mean ± SEM and each dot corresponds to a single value. Scale bars, 100 µm.

646 **Materials and Methods**

647 **Mouse strains**

648 Wild type mice maintained on an ICR/CD-1 background, were used for the *in vivo*
649 experiments, tracing studies and Ca^{2+} imaging. The day on which the vaginal plug was
650 detected was designated as E0.5. The $R26^{Kir2.1\text{-}mCherry}$ mouse line has been described
651 previously (Moreno-Juan et al, 2017) and it was crossed with an inducible thalamic-
652 specific $Gbx2^{CreER}$ line (L. Chen, Guo, & Li, 2009) to generate $Gbx2^{CreER/+}$; $R26^{Kir2.1-}$
653 ^{mCherry} double mutant embryos, referred to as Th^{Kir}. Tamoxifen induction of Cre
654 recombination in the double mutant embryos was performed by gavage administration
655 of tamoxifen (5 mg dissolved in corn oil: Sigma) at E10.5 to specifically target the
656 principal sensory thalamic nucleus. The *Golli-tau-Gfp* mouse line was described
657 previously (Jacobs, 2007) and was crossed with the Th^{Kir} animals. Mutants of either sex
658 were analyzed randomly at stages from P0 to P30. is

659

660 **Histology**

661 For immunohistochemistry, mice were perfused with 4% paraformaldehyde (PFA) in
662 PBS (0.01M), and their brains were removed and post-fixed overnight in the same
663 fixative. Immunohistochemistry was performed on 80 μm vibratome brain sections that
664 were first incubated for 1h at room temperature in a blocking solution containing 1%
665 BSA (Sigma), 2% Donkey Serum (Biowest) and 0.25% Triton X-100 (Sigma) in PBS
666 0.01M. Subsequently, the sections were incubated overnight at 4 °C with the primary
667 antibodies: guinea-pig anti-vGlut1 (1:5000, Synaptic Systems, #135304), chicken anti-
668 GFP (1:3000; Aves Labs, #Gfp-1020) and rat anti-RFP (1:1000 Chromotek, #5F8),
669 rabbit anti-Capasa3a (1:150; Abcam Ab2302). The sections were then rinsed three times
670 in PBS (0.01M) and incubated for 2h at room temperature with secondary antibodies:

671 Alexa-546 donkey anti-rabbit (1:500, ThermoFisher, #A10040), Alexa-488 goat anti-
672 chicken (1:500, ThermoFisher, #A11039), Alexa-594 donkey anti-rat (1:500,
673 ThermoFisher, #A21209), Alexa-488 donkey anti-rabbit (1:500, ThermoFisher,
674 #A21206), Alexa-647 donkey anti-Guinea Pig (1:500, ThermoFisher). Finally, the
675 sections were counterstained with the fluorescent nuclear dye DAPI (Sigma-Aldrich).
676

677 **Tracing of retinal axons**

678 For axonal tracing at postnatal stages, P0 pups were anesthetized under hypothermia.
679 An incision was made over the eyelid of one or both eyes and they were injected with
680 CTB conjugated to Alexa-647 or Alexa-594 (Mol. Probes C34778 or C22842) using a
681 nanoliter injector (WPI). Two, three or seven days later, the animals were perfused with
682 4% PFA in PBS (0.01M), and their brain was dissected out and post-fixed overnight in
683 the same fixative. Vibratome sections (80 µm) were then counterstained with the
684 fluorescent nuclear dye DAPI (Sigma-Aldrich).
685

686 ***In utero* enucleation**

687 For *in utero* enucleation, pregnant females (E14.5) from wildtype colonies or Th^{Kir} mice
688 were administered tamoxifen at E10 and deeply anesthetized with isoflurane to perform
689 laparotomies. The embryos were exposed and both eyes were cauterized in half of the
690 embryos of each litter. The surgical incision was closed and the embryos were allowed
691 to develop until postnatal stages.
692

693 **Calcium imaging in slices**

694 The brains of postnatal mice (P0 and P1) were used for calcium imaging experiments,
695 obtained after they were sacrificed by decapitation. The brains were immediately

696 dissected out and 300 μm coronal vibratome sections (VT1200 Leica Microsystems
697 Germany) were obtained in slicing solution (95% O_2 and 5% CO_2) containing (mM):
698 2.5 KCl, 7 $MgSO_4$, 0.5 $CaCl_2$, 1 NaH_2PO_4, 26 $NaHCO_3$, 11 glucose and 228 sucrose.
699 The slices were placed at room temperature in standard aCSF (119 NaCl, 5 KCl, 1.3
700 $MgSO_4$, 2.4 $CaCl_2$, 1 NaH_2PO_4, 11 glucose) in an atmosphere of 95% O_2 and 5% CO_2.
701 To load the calcium indicator, the slices were incubated at 37 ºC for 30 min in
702 artificial CSF (aCSF) containing 5 μl of Cal520 AM (AAT Bioquest), 1 mM DMSO
703 and 20% pluronic acid. The slices were then placed in a recording chamber with 90%
704 O_2 and 5% CO_2 at 34 ºC and recorded under a Leica DMi8 microscope. We acquired
705 images with Hamamatsu ORCA-Flash 4.OLT camera every 300 ms for 15 minutes. All
706 the calcium imaging data was analyzed as described extensively elsewhere (Moreno-
707 Juan et al., 2017; Antón-Bolaños et al., 2019).
708

709 ***In vivo* extracellular recordings**

710 P6 mice were anesthetized with isoflurane (2.5 %), their scalp was removed and the
711 skull was cleaned. A 3D-printed holder was glued to the skull with cyanoacrylate
712 adhesive and dental cement, and attached to a stereotaxic apparatus. A 2 x 2 mm
713 craniotomy was made over the left hemisphere leaving the dura mater intact. The
714 craniotomy revealed a window above the area of the dLGN (2.0-2.2 mm anterior to
715 lambda and 2.0 mm from the midline) allowing the perpendicular insertion of the multi-
716 channel electrodes. During the recordings, the mice were kept warm (36-37 °C) with a
717 heated blanket and lightly anesthetized with isoflurane (0.5%). Multi-unit activity
718 (MUA, >300Hz) was recorded with a linear 16 channel electrode separated by 50 μm
719 (E16+R-50-S1-L6NT, ATLAS). Shank trajectories were stained with Dil (1,1′-

720 dioctadecyl 3,3,3′,3′-tetramethylindocarbocyanine perchlorate: Invitrogen) diluted in
721 70% alcohol. Probes were inserted perpendicularly, 2800-3000 μm deep for dLGN
722 recordings. The electrical signal activity was sampled at 20 kHz with a filter amplifier
723 and visualized using MC_RACK software (Multi Channel Systems). After the
724 recording sessions, the animal's brain was dissected out and fixed overnight in 4% PFA.
725 In order to determine the position of every channel, 100 μm thick coronal sections were
726 counterstained with the fluorescent nuclear dye DAPI (Sigma-Aldrich) and the data was
727 analyzed using Matlab™ routines.

728 **Dark reared experiments**

729 For the dark reared experiments, *Th*^{Kir} animals and their control littermates were put
730 into a completely dark environment with their mother from P5 to P15. After this time
731 the animals were rapidly perfused with 4% PFA in PBS (0.01M). The animal's brain
732 was dissected out and post-fixed overnight in the same fixative. Vibratome sections (80
733 μm) were then subjected to immunohistochemistry.

734

735 **Data analysis and statistics**

736 The analysis of the calcium imaging experiments was described in detail elsewhere
737 (Moreno-Juan et al., 2017; Antón-Bolaños et al., 2019). ImageJ software was used to
738 quantify CTA and RTA invasion of the dLGN. Coronal slices (80 μm) were obtained
739 from the animals subjected to the different conditions and immunostained for vGlut1 or
740 GFP. At least three dLGN sections were analyzed from each animal, correcting for the
741 fluorescence background. Threshold images of the fluorescence were analyzed by
742 ImageJ software, analyzing the particles of the pixels that cover the dLGN and
743 measuring the proportion of pixels occupied by CTAs in the dLGN.

744 Caspase3a positive cells were quantified in coronal sections (80 μm) and normalized
745 to the area of each dLGN. The whole dLGN was measured from P3, P4 and P6 control
746 and Th^{Kir} mice, and the results were normalized to the mean of the controls,
747 representing the fold-change in Caspase3a positive cells in the Th^{Kir} mice.
748 Statistical analysis was carried out in GraphPad Prism6™ and Matlab™, and the
749 data are presented as the mean and SEM. Statistical comparison between the groups was
750 performed using an unpaired two-tailed Student's *t* test and when the data failed a
751 Kolmogorov-Smirnov or a Shapiro Wilk test of normality, a two-tailed, non-parametric
752 Mann-Whitney U-test was used. A Two-way ANOVA test was performed on the
753 embryonic enucleation in Th^{Kir} mice and for the DR experiments. No statistical methods
754 were used to predetermine the sample size, but our sample sizes are considered
755 adequate for the experiments and consistent with the literature (Brooks et al., 2013;
756 Grant et al., 2016; Seabrook et al., 2013). The mice were not randomized.
757

758 **Figure 1**

759 Figure 1D Event frequency: control 0.27 ± 0.03, n = 7; Th^{Kir} 0.02 ± 0.005, n = 5
760 (***P<0.001 Two-tailed student's *t*-test). Wave frequency in dLGN: control 0.34 ±
761 0.04, n = 7; Th^{Kir} 0 ± 0, n = 5 (**P=0.0025, Mann-Whitney *U*-test).
762 Figure 1H Firing rate dLGN: control 0.16 ± 0.05, n = 6; Th^{Kir} 0.07 ± 0.12, n = 8
763 (*P=0.04 Mann-Whitney *U*-test).

764 **Figure 2**

765 Figure 2B vGlut1 at P4: control 10 ± 1%, n = 5; Th^{Kir} 1.67 ± 0.34%, n = 5 (***P<0.001
766 Two-tailed student's *t*-test). At P6: control 35.96 ± 4.47%, n = 5; Th^{Kir} 1.24 ± 0.51%, n
767 = 5 (***P<0.001, Two-tailed student's *t*-test). At P9: control 62.4 ± 4.49%, n = 5; Th^{Kir}
768 12.15 ± 0.74%, n = 3 (***P<0.001, Two-tailed student's *t*-test).

769 **Figure 3**

770 Figure3A dLGN size at P0: 84326 ± 2872, *n* = 4; Th^{Kir} 83720 ± 2498, *n* = 6 (P=0.88,

771 Two-tailed student's *t*-test). At P3: 89800 ± 4558, *n* = 3; Th^{Kir} 80403 ± 2300, *n* = 5

772 P=0.14, Mann-Whitney *U*-test. P4: 118410 ± 6262, *n* = 4; Th^{Kir}: 79748 ± 4351, *n* = 4

773 (*P=0.02, Two-tailed student's *t*-test). At P6: 193136 ± 5603, *n* = 5; Th^{Kir} 92022 ±

774 3380, *n* = 5 (***P<0.001, Two-tailed student's *t*-test).

775 Figure 3C Caspase3A^{+} cells normalized to the control data at P3: control 100 ± 14.97%,

776 *n* = 3; Th^{Kir} 816.3 ± 122.3%, *n* = 5 (*P=0.03, Mann-Whitney *U*-test). At P4 control 100

777 ± 30.98%, *n* = 4; Th^{Kir} 684.4 ± 139.2%, *n* = 4 (*P=0.028, Mann-Whitney *U*-test). At P6

778 control 100 ± 7.71%, *n* = 6; Th^{Kir} 762.6 ± 87.69%, *n* = 6 (***P<0.001, Two-tailed

779 student's *t*-test).

780 **Figure 4**

781 Figure 4D Percentage of RTAs in dLGN at P2. Contralateral RTAs in dLGN, control:

782 69.94 ± 1.56%, *n* = 3; Th^{Kir}: 66.5 ± 1.74%, *n* = 4. P=0.22 Two-tailed student's *t*-test.

783 Ipsilateral RTAs in dLGN control: 20.45 ± 2.27%, *n* = 3; Th^{Kir}: 24.34 ± 2.3%, *n* = 4.

784 P=0.29 Two-tailed student's *t*-test.

785 **Figure 5**

786 Figure 5B Event frequency: control 0.08 ± 0.02, *n* = 5; embBE 0.23 ± 0.02, *n* = 5

787 (***P<0.0005, Two-tailed student's *t*-test). Wave frequency in dLGN: control 0.08 ±

788 0.03, *n* = 5; embBE 0.31 ± 0.03, *n* = 5 (*P=0.01, Mann-Whitney *U*-test).

789 Figure 5F % of CTAs in the dLGN at P1: control 3.26 ± 0.2%, *n* = 3; embBE 8.85 ±

790 1.44%, *n* = 3 *P=0.018, Two-tailed student's *t*-test). At P3: control 12.86 ± 1.59%, *n* =

791 4; embBE 53.92 ± 5.05%, *n* = 6 (***P<0.001, Two-tailed student's *t*-test). At P7:

792 control 43.89 ± 2.46%, *n* = 4; embBE 74.82 ± 1.68%, *n* = 5 (*P=0.01, Mann-Whitney

793 *U*-test).

794 Figure 5I % of vGlut1 in the dLGN at P7: control *n* = 5, embBE n= 5, Th^{Kir} n=3, Th^{Kir}
795 embBE n= 4. A two-way ANOVA test with Tukey's post hoc analysis indicates that the
796 interaction between all the conditions are significant, comparisons: control vs Th^{Kir} ***
797 P<0.001; control vs embBE *** P<0.001; control vs Th^{Kir} embBE *P=0.01; Th^{Kir} vs
798 embBE *** P<0.001; Th^{Kir} vs Th^{Kir} embBE *** P<0.001; embBE vs Th^{Kir}embBE **
799 P=0.0025.

800 **Figure 6**

801 Figure 6A %vGlut1 in the dLGN of P10: control 79.28 ± 2.31%, *n* = 7; Th^{Kir} 18.85. ±
802 1.85%, *n* = 6 (***P<0.001, Two-tailed student's *t*-test).

803 Figure 6B %vGlut1 in the dLGN of P13: control 76.62 ± 1.23%, *n* = 5; Th^{Kir} 76.69. ±
804 0.8%, *n* = 5 (P=0.96, Two-tailed student's *t*-test).

805 Figure 6E % of vGlut1 in the dLGN at P15: control *n* = 3, control DR n= 5, Th^{Kir} n=3,
806 Th^{Kir} DR n= 6. A two-way ANOVA test with Tukey's post hoc analysis, comparisons:
807 control vs Th^{Kir} P= 0.97; control vs control DR P= 0.99; control vs Th^{Kir} DR
808 ***P<0.005; Th^{Kir} vs control DR P= 0.99; Th^{Kir} vs Th^{Kir} DR *** P<0.001; control DR vs
809 Th^{Kir} DR *** P<0.001.

810 **Figure S2**

811 Figure S2B $Nissl^{+}$ cells/100 μm^2: control 110.5 ± 4.29, *n* = 4; Th^{Kir} 124.8 ± 6.34%, *n* =
812 4 (P=0.11. Mann-Whitney *U*-test).

813 **Figure S3**

814 Figure S3A %CTAs in the dLGN of P2 mice: control 7.28 ± 2.24%, *n* = 4; embBE 39.3
815 ± 3.1%, *n* = 4 (*P=0.02, Mann-Whitney *U*-test).

816 Figure S3B % of vGlut1 in the dLGN at P2: control 7.1 ± 9.92%, *n* = 3; embBE 44.32±
817 2.35%, *n* = 3 (***P<0.001, two-tailed student's *t*-test).

818 Figure S3C % of vGlut1 in the dLGN at P3: control 10.68 ± 1.92%, *n* = 3; embBE

819 53.06 ± 4.41%, *n* = 3 (***P<0.001, two-tailed student's *t*-test).

820 Figure S3D % of vGlut1 in the dLGN at P7: control 39.01 ± 3.03%, *n* = 3; embBE

821 71.45 ± 1.11%, *n* = 3 (***P<0.001, two-tailed student's *t*-test).

822 **Figure S4**

823 Figure S4A %vGlut1 at P30: control 87.26 ± 3.36%, *n* = 3; Th^{Kir} 87.16. ± 3.28%, *n* = 3

824 (P=0.98, two-tailed student's *t*-test).

825 Figure S4B %vGlut1 at P14: control 93.17 ± 1%, *n* = 3; Th^{Kir} 89.31. ± 1.16%, *n* = 3

826 (P=0.1, two-tailed student's *t*-test).